Research Square

Preprints are preliminary reports that have not undergone peer review.
They should not be considered conclusive, used to inform clinical practice,
or referenced by the media as validated information.

Re-growth and doping effects on ZnO nanorod UV photodiodes

Mohadeseh Pasdar
Malek Ashtar University of Technology
Rouhollah Azimirad
azimirad@yahoo.com

Malek Ashtar University of Technology
Fatemeh Dehghan Nayeri
Malek Ashtar University of Technology
Farhad A. Boroumand
K. N. Toosi University of Technology
Sadegh Babaei
Malek Ashtar University of Technology
Seyedeh Somayeh Miri
K. N. Toosi University of Technology

Article

Keywords:

Posted Date: November 20th, 2026

DOI: https://doi.org/10.21203/rs.3.rs-11496977/v1

License: This work is licensed under a Creative Commons Attribution 4.0 International License.
Read Full License

Additional Declarations: No competing interests reported.

Re-growth and doping effects on ZnO nanorod UV photodiodes

Pasdar, Mohadeseh[†, 1]

Azimirad, Rouhollah[†*, 1]

Dehghan Nayeri, Fatemeh[†*, 1]

Boroumand, F. A.[*, 2]

Babaei, Sadegh[‡, 1]

Miri, Seyedeh Somayeh[‡, 3]

[1]Faculty of Electrical & Computer Engineering, Malek-Ashtar University of Technology, Tehran, 1774-15875, Iran

[2]Organic Electronics Lab., Department of Electrical Engineering, K. N. Toosi University of Technology (KNTU), Tehran, 1355-16315, IRAN

[3]Electronics Lab., Department of Electrical Engineering, K. N. Toosi University of Technology (KNTU), Tehran, 1355-16315, IRAN

[†] Corresponding authors: m.pasdar@eetd.kntu.ac.ir, azimirad@mut.ac.ir, azimirad@yahoo.com, f.d.nayeri@mut.ac.ir

[*] These three authors contributed equally as second authors.

[‡] These two authors contributed equally as third authors.

Key words and phrases. Zinc oxide, UV photodiode, Regrowth, Doping.

Abstract. Zinc oxide (ZnO) nanorods are promising candidates for ultraviolet (UV) photodetectors; however, simultaneous optimization of dark current and sensitivity remains challenging. In this study, ZnO nanorods with diameters of 25-50 nm were synthesized via a hydrothermal method, and the effects of diameter, Gd doping, and regrowth (secondary growth) on detector performance were systematically investigated. The 25 nm undoped single-step sample exhibited the highest sensitivity, external quantum efficiency (EQE), responsivity, and detectivity, all of which degraded with increasing diameter. In contrast, the re-grown 50 nm sample achieved the lowest dark current (-0.9 μA at -10 V), attributed to improved crystallinity and reduced bulk defect density achieved through the re-growth process, which suppresses the generation-recombination current the dominant leakage mechanism under reverse bias. The Gd-doped 35 nm sample consistently showed the poorest performance. These findings reveal a key trade-off: diameter reduction maximizes photodetection metrics, while re-growth effectively suppresses dark current via bulk defect engineering. The 25 nm sample is optimal for high-sensitivity applications, whereas the 50 nm re-grown sample is suitable for low-noise devices. This work provides a pathway for designing application-specific ZnO nanorod UV photodetectors.

1. Introduction

In recent decades, a diverse range of wide-bandgap semiconductors have been investigated and received considerable attention. Among the most thoroughly studied candidates for UV detection are zinc oxide (ZnO) and its nanostructures. This semiconductor exhibits high chemical stability, remarkable optical transparency, and excellent thermal stability. ZnO nanowires have also garnered considerable attention, owing to their high surface-to-volume ratio, efficient charge transfer, and strong light-matter interaction. These types of detectors have been realized in various architectures, including photoconductors, Schottky diodes, p-n and p-i-n junctions, MSM (metal- semiconductor-metal) structures, and phototransistors [1]. Chen et al. [2] demonstrated that the structural quality and functional performance of ZnO-based devices and their nanostructures can be effectively improved through various processing methods. Ahsan et al. [3] have highlighted the critical importance of evaluating key performance metrics in photodetectors, including responsivity, detectivity, response time, and external quantum efficiency (EQE). Ülkü et al. [4] have reported that improving photodetector performance through

dark current suppression is of critical importance and practical efficacy. To this end, various techniques have been employed, which can be broadly categorized into three levels: material engineering, device design, and thermal management. Soylu and Simsek [5], for instance, demonstrated that the use of sulfur-containing organic compounds can lead to reduced surface roughness, enhanced UV light absorption, and ultimately improved electrical performance of the device.

TABLE 1. Ratio of precursors, Doping and Regrowth of samples S_1 to S_4

Sample No.	Ratio of precursors	Doping	Re-growth
S_1	1:15	None	0
S_2	1:10	None	0
S_3	1:10	Gd (3%wt)	0
S_4	1:10	None	1

Shahat et al. [6] also demonstrated that the incorporation of Al_2O_3 nanoparticles into ZnO leads to a notable enhancement in ultraviolet absorption. On the other hand, Shang et al. [7] have pointed out that for photodetectors fabricated from materials other than ZnO, such as perovskites, the primary challenges remain stability and toxicity, which are considered key issues in this research area. Peng et al. [8] have also reported that photodetectors employing double-heterojunction architectures exhibit substantially improved responsivity and quantum efficiency. Despite these advances, the combined effects of dimensional engineering, doping, and multi-step growth on the overall performance of ZnO nanorod-based photodetectors have not yet been systematically investigated. Building upon our previous work [9] on dimension tuning without doping, we investigated the combined effects of Gd doping and re-growth on ZnO nanorods (25-50 nm). The re-growth process was performed on the as-grown nanorods via a secondary hydrothermal step to improve crystallinity and reduce bulk defect density. Our results reveal that re-growth suppresses dark current via bulk defect engineering, while diameter reduction enhances sensitivity, EQE, responsivity, and detectivity.

2. EXPRIMENTAL DETAILS

2.1. **Synthesis.** In the process of fabricating an ultraviolet detector, p-type silicon substrates were first placed in pure sulfuric acid at a temperature of 60^oC. Hydrogen peroxide was also added to the above solution at specific intervals to initiate the bubbling process

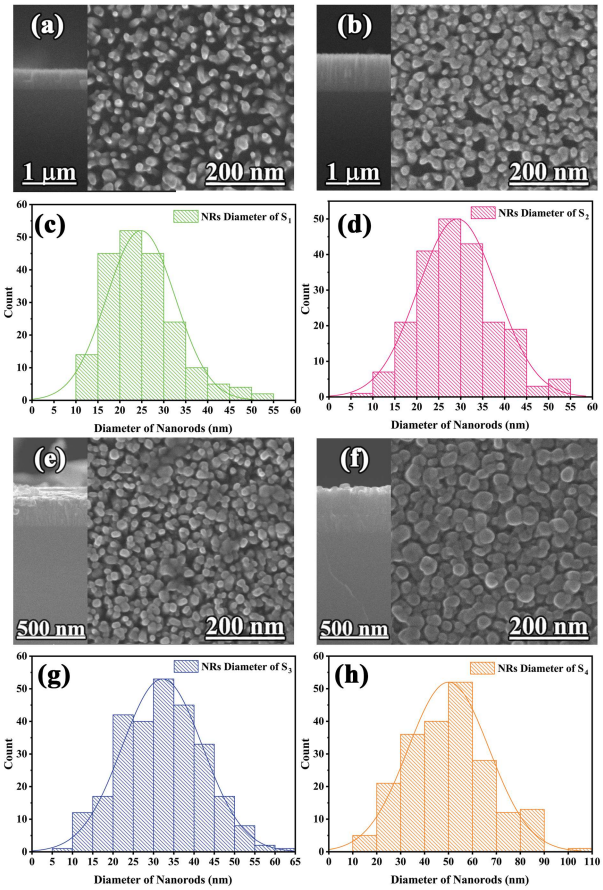


FIGURE 1. FE-SEM images of surface, cross-section and histogram of the samples

and clean the substrate surface. Finally, the silicon substrates were immersed in deionized water and then dried with nitrogen gas. Radio-frequency (RF) sputtering was used to create seeds on the silicon substrate. With this method, a very thin and high-quality layer of zinc oxide was deposited on the surface of the substrate.

This seed-creation method can result in high-quality growth of zinc oxide nanostructures. It also enables high quality and a uniform and relatively precise thickness for the seed layer by precisely controlling pressure, temperature, and process speed.

After this step, the substrate was prepared for optimal growth of zinc oxide nanorods. The prepared substrates were immersed in a solution of zinc nitrate hexahydrate and sodium hydroxide, and the solution temperature was set to 70^oC. The substrates were placed in the solution for 90 minutes and then removed from the bath. Subsequently, they were washed with deionized water and dried under nitrogen gas. In this work, the growth of zinc oxide nanorods was carried out by the hydrothermal method. Table 1 shows the ratio of precursors and growth conditions for each sample.

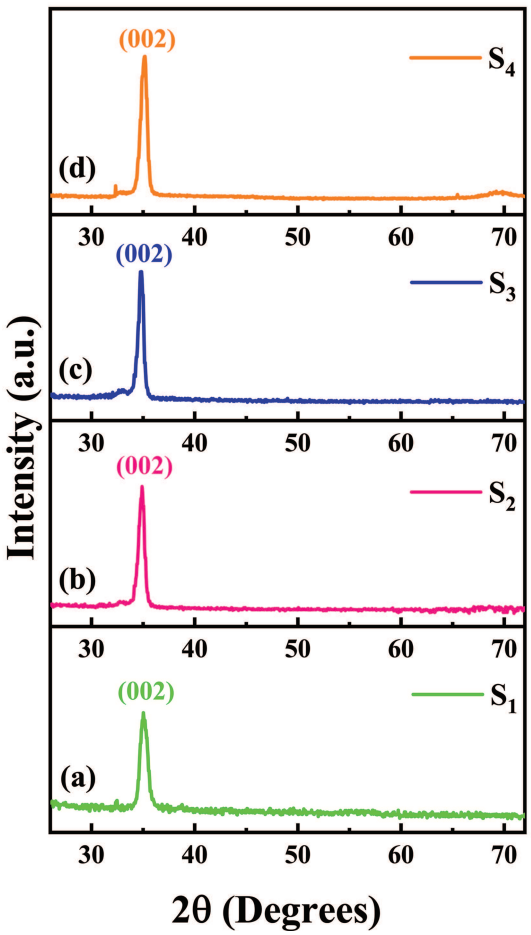


FIGURE 2. XRD spectrum of four samples, a) S_1, b) S_2, c) S_3, and d) S_4

The growth of zinc oxide nanorods in samples S_1, S_2, and S_3 was carried out in only one step. In sample S_4, the nanorods were regrown in two stages. Sample S_1 also had exactly the same growth conditions as sample S_2, except that the precursor ratio in S_1 was changed.

TABLE 2. Diameter, length and diameter to length ratio of samples S_1 to S_4

Sample No.	Diameter (nm)	Length (nm)	Diameter/Length ratio
S_1	25	380	0.06
S_2	30	730	0.04
S_3	35	280	0.12
S_4	50	440	0.11

2.2. **Measurements.** The structural and morphological characteristics of the samples were examined by field emission scanning electron microscopy (FE-SEM, MIRA3, TESCAN). Also, XRD of the samples was performed using a PHILIPS PW 1730 device with

Cu $K\alpha$ radiation. The electrical characteristics of these devices were obtained under UV laser irradiation using a 4145B Semiconductor Parameter Analyzer, HP. Optical parameters were also measured by PL characterization using a Perkin Elmer LS55 device under an excitation wavelength of 330 nm. In this study, an ultraviolet excitation source with a power of 5 mW and a wavelength of 365 nm was used. This laser was located at a distance of 5 cm and at an angle of 45 degrees from the sample.

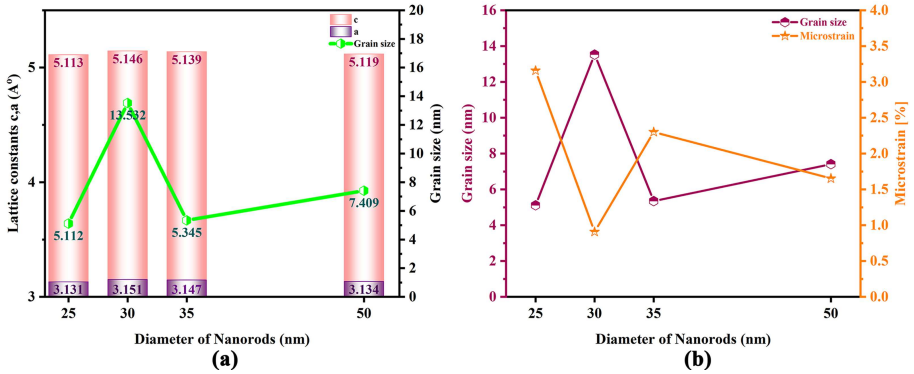


FIGURE 3. XRD results: a) c/a and Grain size changes and b) comparison Grain size and Microstrain

3. Results and discussion

3.1. **FE-SEM observation.** Figure 1a, ab, 1e, and 1f show the FE-SEM images of the four samples. The diameter of the nanorods of the samples varies between 25 and 50 nm. Due to the small diameter of the nanorods and in order to more accurately determine the average diameter values, diameter distribution graphs were calculated for each sample, which can be seen in Figure 2. The average diameter values of the samples in each sample were extracted from the results in Figure 1c, 1d, 1g, and 1h and are listed in Table 2. Figure 1 clearly shows that due to the small diameter of the nanorods in the four samples and the resolution of the FE-SEM images, the average diameter changes of the zinc oxide nanorods are very close to each other and very different changes are not observed in samples with different conditions. The nanorods of the two samples S_1 and S_2 were grown on the substrate in a single step and under the growth method and conditions described in the previous section, and have an average diameter between 25 and 30 nm. The only difference between these two samples is the concentration of the precursors [9, 10, 11], and this slight change in concentration did not have a significant effect on the size of the nanorods, especially their diameter. The nanorod diameter distribution graphs of samples S_1 and S_2 in Figure 1c, 1d, 1g, and 1h also indicate the

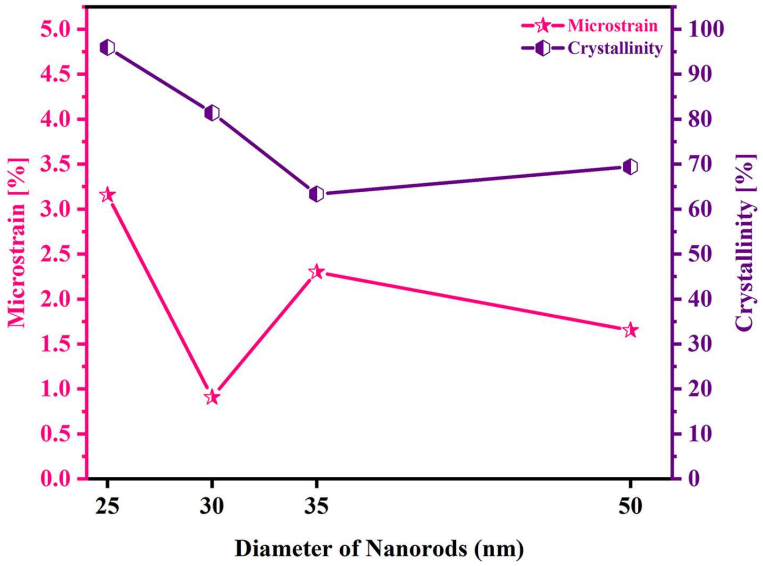


FIGURE 4. comparison Microstrain and crystallinity of four samples according to diameter changes

similarity of the frequency of nanorods in the range specified in the graph. The diameter of the nanorods in sample S_3 is larger than the diameter of the nanorods in sample S_2 with similar growth conditions, due to the doping of the nanostructure with the element gadolinium (Gd) [12, 13]. Sample S_4 also has the largest diameter of nanorods among the four samples due to the regrowth of nanorods on the initial nanostructure and under the same growth conditions [14]. As can be seen in Figure 1f and the cross section of the FE-SEM images, the interface resulting from the two growth steps in sample S_4 is clearly visible. In addition, the length of the nanorods of this sample can also be measured, as shown in Table 2.

3.2. **X-ray observation.** The XRD pattern of zinc oxide nanorods for four samples S_1, S_2, S_3, and S_4 is shown in Figure 2. This pattern clearly confirms the existence of a wurtzite hexahedral phase with the space group P_3^6mc. On the other hand, the intensity of the (002) peak is very high, indicating a strong orientation of the nanorods along the c-axis of the nanostructure and perpendicular to the substrate surface [15, 16]. If the 2θ angles corresponding to the original (002) peak are considered for samples S_2 and S_3, which have similar growth conditions and the only difference is the Gd doping in sample S_3, it is observed that the peak of the doped sample will shift to the right [17, 18]. That is:

$$2\theta_{S_3}(34.88) > 2\theta_{S_2}(34.83)$$

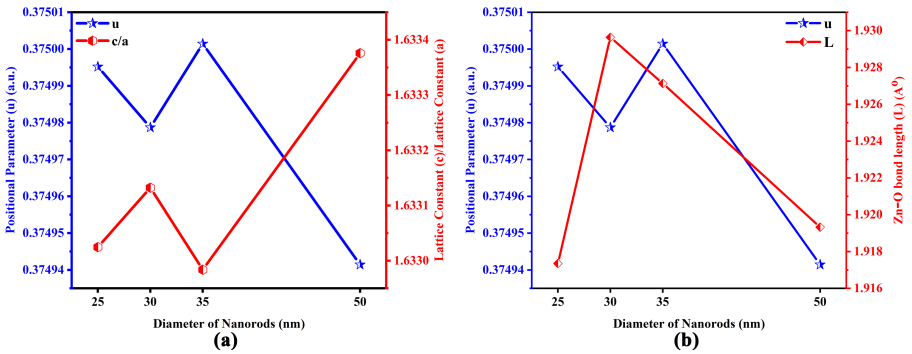


FIGURE 5. Calculated values to check bond length changes: a) comparison of $c/\ a$ and u changes according to the diameter of the samples and b) comparison of u and L values according to the diameter changes of the four samples

TABLE 3. c/a and dislocation density of samples

Sample No.	c/a	$\sigma\ (m^{-2})$
S_1	1.63302	38.26×10^{15}
S_2	1.63313	5.46×10^{15}
S_3	1.63298	34.99×10^{15}
S_4	1.63338	18.21×10^{15}

To quantitatively evaluate the effects of size and strain, the Williamson-Hall and Debye-Scherrer models were used. The closeness of the dislocation density values $\sigma = 1/D^2$ (D is grain size.) and the lattice parameter c/a (Table 3), which are close to the ideal values of wurtzite, also indicates the low structural defects and favorable crystallinity of the synthesized samples.

The changes in the lattice parameters c and a, grain size, and microstrain can be seen in Figure 3a and Figure 3b. The appearance of very small peaks in the XRD spectrum could be a factor contributing to the reduced grain size and crystallinity of S_4 compared to S_2, given that the growth conditions for both samples were identical and only S_4 underwent regrowth [19].

A comparison of the microstrain and grain size values in Figure 3b reveals that, among samples S_2, S_3, and S_4-which share the same precursor concentration-the highest microstrain is observed in sample S_3 (Gd-doped). The presence of Gd within the structure has caused lattice distortion and an increase in microstrain [20]. In sample S_3, no secondary

peak appeared; however, Gd doping in the nanostructure induced lattice disorder and reduced crystallinity. Additionally, the grain size decreased [21].

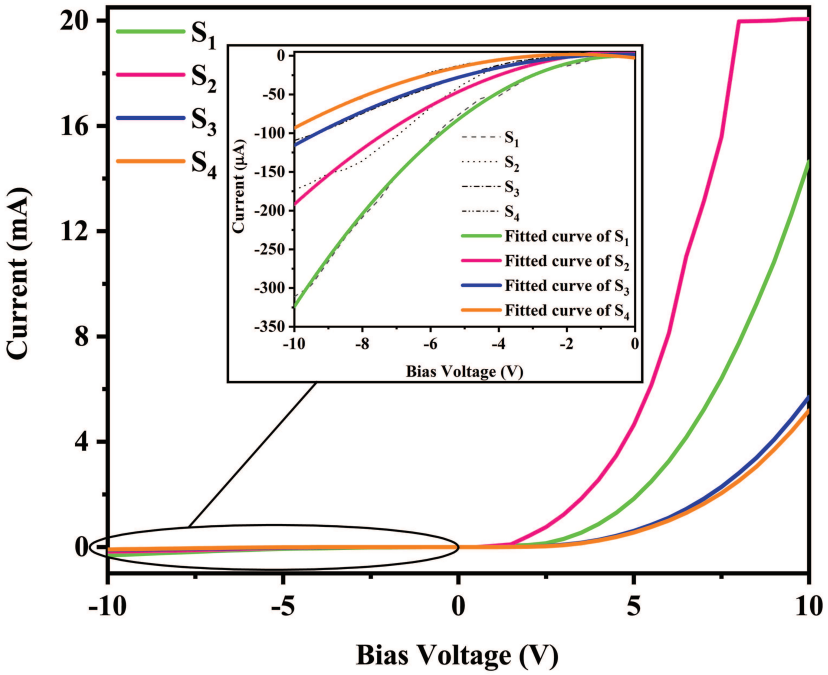


FIGURE 6. I-V characteristic diagrams of samples S_1 to S_4 under UV laser exposure. (The inner figure corresponds to the magnification of the curves in reverse bias.)

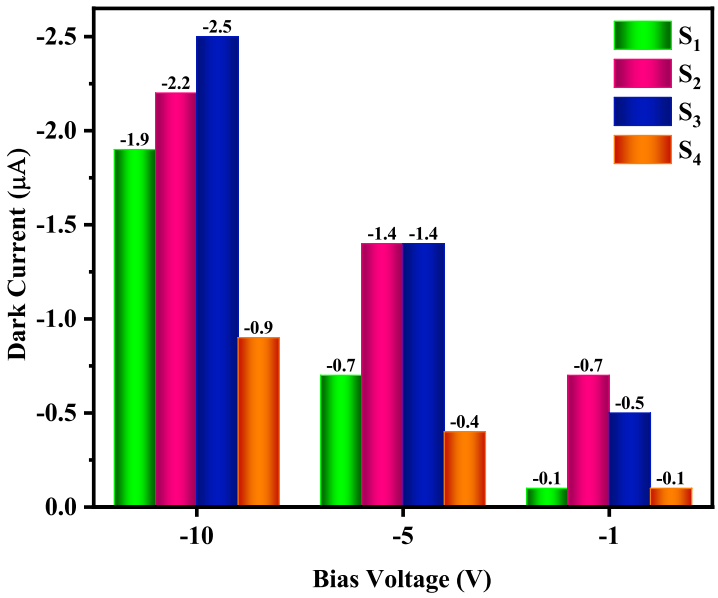


FIGURE 7. Dark current diagrams of samples S_1 to S_4 in three reverse biases.

Furthermore, an analysis of microstrain and crystallinity variations across the four samples revealed that, among the undoped samples (S_1, S_2, and S_4), the highest crystallinity was observed in sample S_1. The enhanced crystallinity in this sample is attributed to the reduced concentration of precursors; lower concentrations facilitate more controlled growth and prevent the formation of structural defects [22].

It is usually expected that microstrain will decrease as crystallinity improves in the structure. However, in these samples, S_1, with the highest crystallinity, has the highest microstrain. Therefore, other involved parameters had to be examined. In Figures 5a and 5b, the position parameter u and the length of $Zn--O$ bonds in each sample were calculated. The calculations showed that the shorter the $Zn--O$ bond length in the nanostructure compared to the value calculated for a zinc oxide unit cell (1.9767 $\mathring{A}$), the greater the microstrain in that structure [23, 24]. A complete explanation of this has been provided in our previous work [9].

$$u = \frac{a^2}{3c^2} + 0.25 \tag{3.1}$$

where u, a, and c are the positional parameter in the wurtzite structure, lattice constant, and lattice parameter, respectively.

$$L = \sqrt{\left(\frac{a^2}{3} + \left(\frac{1}{2} - u\right)^2 c^2\right)} \tag{3.2}$$

where L is the $Zn--O$ bond length [24]. This explains the microstrain changes in the three undoped samples. The Gd-doped sample (S_3) exhibits the lowest crystallinity and a relatively high microstrain. An analysis of the $Zn--O$ bond length revealed no significant deviation from the reference value; therefore, the increased microstrain in this sample stems from another factor. Calculations of dislocation density showed an increase compared to sample S_2 -which was grown under similar conditions but is undoped- indicating that Gd doping leads to a reduction in grain size and a consequent rise in dislocation density ($\sigma_{S_3} > \sigma_{S_2}$) [20].

3.3. **I-V characteristics.** The electrical parameters of the fabricated devices were measured in the dark and under UV light, and the I-V illumination curves of the four samples can be seen in Figure 6. The I-V values in the dark (Figure 7), under UV light (Figure

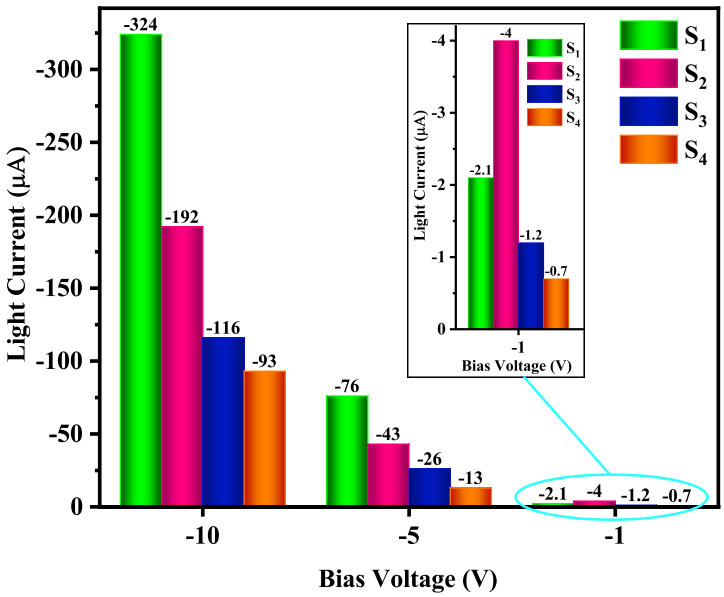


FIGURE 8. Light current diagrams of samples S_1 to S_4 in three reverse biases.

8) and photocurrent (Figure 9) are determined at three different reverse bias voltages of -1 V, -5 V and -10 V.

Sample S_1 has the smallest diameter among the four samples, which, according to our previous work, proved that by reducing the diameter of the grown nanorods, the dark current will also decrease significantly, and this condition applies to the three samples S_1, S_2, and S_3, which were grown in only one step.

On the other hand, the increase in dark current for sample S_3 compared with sample S_2 is attributed to Gd doping of the nanostructure, which enhances conductivity [25], thereby increasing the dark current of the device. However, for sample S_4, despite the regrowth and increased diameter of the nanorods compared with the other samples, the dark current did not increase; instead, it reached the lowest value among the four samples. The reduction in dark current in this sample is attributed to improvements in crystal quality and interface quality, which can be explained by reductions in defect density and lattice mismatch, respectively [26, 27]. Figure 8 shows a downward trend in the photocurrent from sample S_1-S_4, which is attributed to a decrease in internal optical gain. The sample with the smallest diameter exhibits the greatest increase in the surface-to-volume ratio; consequently, because of the presence of surface defects, a stronger radial electric field is generated. This field facilitates effective separation of photogenerated

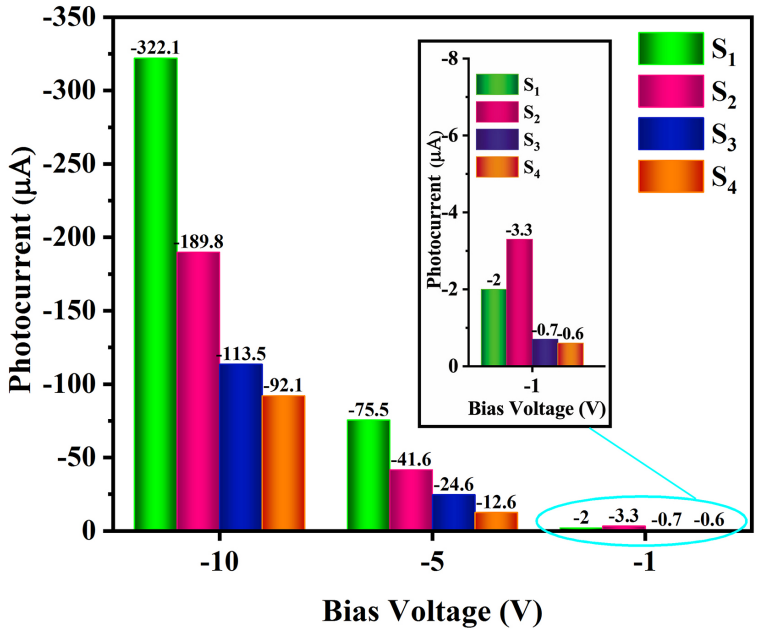


FIGURE 9. Photocurrent diagrams of samples S_1 to S_4 in three reverse biases.

electron-hole pairs, leading to an increase in internal optical gain [28]. The calculated photocurrents for the four samples at three different reverse bias voltages are shown in Figure 9. These currents were obtained using the relationship $I_{Ph} = I_{Ligth} - I_{Dark}$.

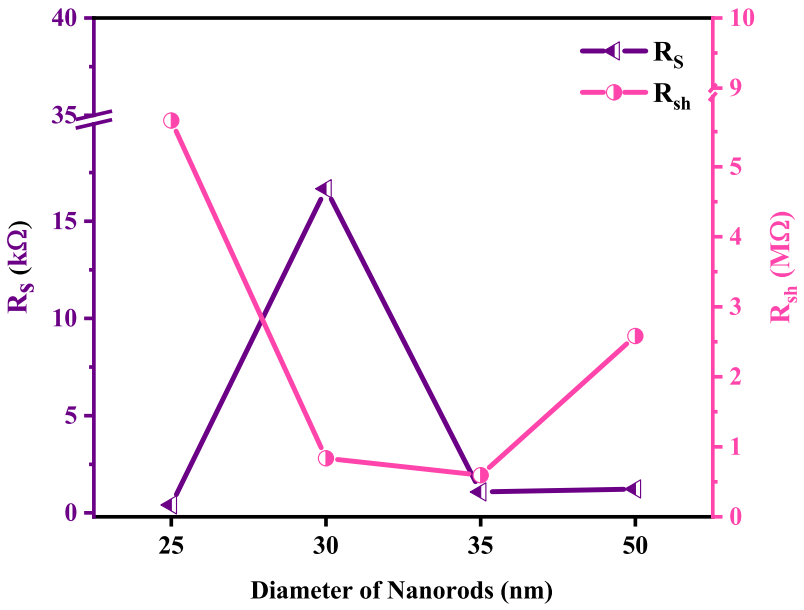


FIGURE 10. Series and shunt resistances of samples S_1 to S_4.

Figure 10 shows that, for all samples, the series and shunt resistance values are highly favorable, indicating high structural quality and reproducibility of the growth process.

Sample S_1, which exhibits the lowest R_s and the highest R_{sh}, is the best-performing sample in terms of enhanced conductivity and reduced leakage current. Notably, Gd doping in sample S_3 successfully improved conductivity [25], resulting in a lower R_s than that of sample S_2. Sample S_4 also exhibits low Rs and significant shunt resistance-attributed to improved structural crystallinity-and can likewise be considered a favorable sample. In contrast, R_s values reported in other studies-covering both undoped and doped conditions-are significantly higher than the series resistance observed in the S_1-S_4 photodiodes [25, 29, 30]. In this study, the ideality factors for photodiodes S_1-S_4 were determined to be 7.17, 9.1, 11.92, and 15.73, respectively values that differ from those reported elsewhere. For instance, ideality factor (n) values reported for undoped samples in other studies include $\sim$ 1 [29], 2.01 [25], 3.18 [31], and $\sim$ 11 [32]. Other reports [25, 30] present ideality factor values for Gd-doped structures at various concentrations that are lower than the value obtained for sample S_3. To further evaluate device performance, operational parameters-including responsivity, detectivity, and external quantum efficiency (EQE)-were calculated. Figure 11 and Figure 12 show the response at reverse bias voltage level of -10 V.

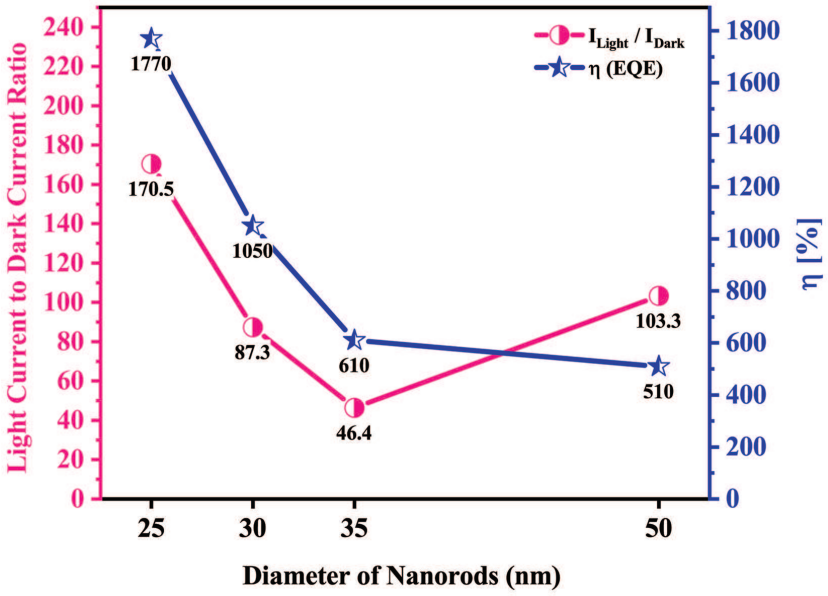


FIGURE 11. Sensitivity (light current to dark current ratio) and *EQE* of samples in -10 V.

The values presented in Figures 11 and 12 demonstrate the desirable intrinsic sensitivity of the devices. To assess the switching performance of the devices, the photocurrent-to-dark-current ratio was also calculated (Figure 11). Figure 11 illustrates the high sensitivity of the devices in distinguishing light from darkness, with sample S_1 exhibiting

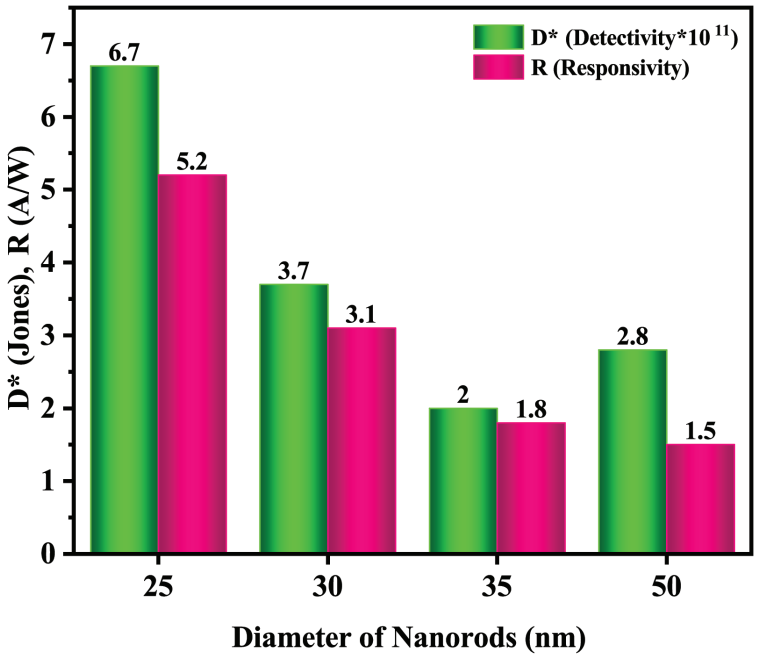


FIGURE 12. Detectivity, and Responsivity of samples in -10 V.

the highest value. Among the four samples, S_1 demonstrated the best performance in terms of both responsivity (Figure 12) and sensitivity (Figure 11). Figure 12 displays the detectivity of the devices, demonstrating their high signal-detection capability in the presence of noise. The calculated EQE shown in Figure 11 indicates that sample S_1 exhibits the best performance in terms of photon-to-electron conversion.

A comparison of the detectivity values obtained in this work with those reported in [30, 33] reveals an improvement in detectivity, attributable to reduced dark current and increased responsivity in sample S_1. Furthermore, the EQE results for samples S_1-S_4 indicate high internal efficiency, contrary to one report [34]. In contrast, higher values have been reported elsewhere [30, 35], which were attributed to the hybrid structure and gallium doping of the nanostructure. Although the sensitivity of sample S_1 was nearly double the reported value (90) [36], other reports indicate sensitivities higher than that obtained here [37, 38]. For the undoped case, responsivity values reported elsewhere are 0.219 A/W [31], 0.23 A/W [34], 293 mA/W [39], 0.38 A/W [40], 0.5 A/W [41], and 8.14 A/W [35], whereas the Gd- doped structure yielded 28 A/W under white light [33]. These values indicate that, despite its good performance under white light, the Gd-doped device did not exhibit comparable performance in the UV range.

3.4. **PL spectroscopy.** Figure 13 shows the PL characteristic of sample S_1. The PL spectroscopy results of the first sample reveal the luminescent properties of zinc oxide

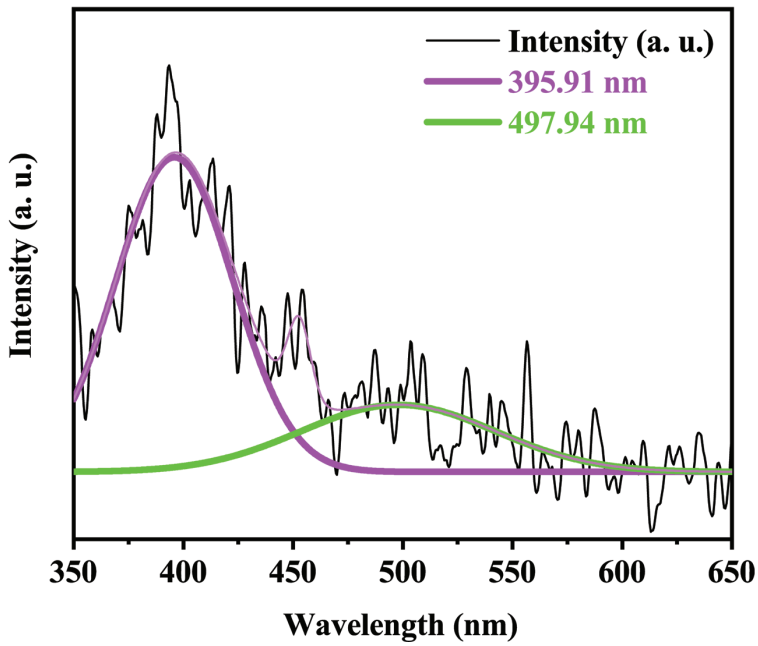


FIGURE 13. PL spectra and the peaks obtained from fitting of S_1. (The peak corresponding to each emission is marked with the same color.)

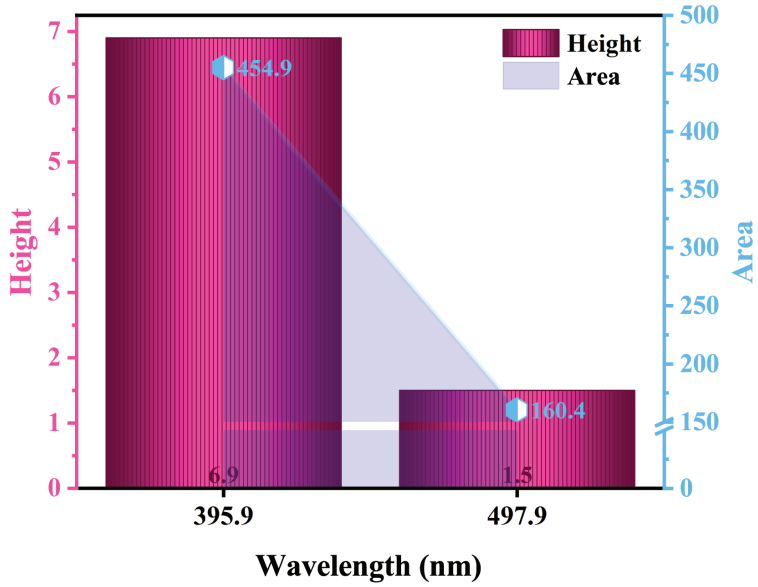


FIGURE 14. Height and area under the curve of the two violet and green peaks of S_1.

nanorods. In the curve of this sample, two peaks were fitted in the UV and visible regions [42]. In the UV region, the high intensity of violet emission at a wavelength of 395.9 nm after spectrum fitting indicates the high emission of zinc oxide nanorods at these wavelengths, which occurred due to excitonic recombination [43]. It is this inherent and distinctive feature of zinc oxide and its nanostructures that makes this material attractive and useful for UV spectrum detection applications.

The broad green peak centered at approximately 500 nm also indicates oxygen vacancies in the zinc oxide nanostructure [44]. This phenomenon occurs due to the transition between trap levels associated with zinc and oxygen vacancies in zinc oxide [42]. It can also be caused by the transition between deep donor traps dependent on defects of interstitial zinc atoms with the zinc oxide band [43]. In Figure 14, the peak height and area under the curve of the two violet and green peaks are shown. The low intensity (peak height) and area of the green emission peak compared to the intensity (peak height) and area of the violet emission peak indicate a reduction in defects and, consequently, an improvement in the crystallinity of zinc oxide nanorods in this nanostructure.

4. Conclusion

A fundamental trade off exists in ZnO nanorod UV photodetectors. Reducing the diameter to 25 nm (single step growth) maximizes sensitivity, EQE, and responsivity, while the re-grown 50 nm sample achieves the lowest dark current (-0.9 μA at -10 V) by effectively suppressing bulk generation-recombination defects via re-growth, which overcomes the moderate shunt resistance reduction. Gd doping uniformly deteriorates all performance metrics. Thus, the 25 nm single-step sample is optimal for high sensitivity applications, whereas the 50 nm re-grown sample is preferred for low noise operation. This diameter defect engineering strategy provides a practical framework for designing application-specific ZnO-based UV photodetectors.

Data Availability

All data generated or analysed during this study are included in this published article.

References

[1] Jehad, A.K., Akalin, S.A., Erol, M., Ozturk, Y. and Yurddaskal, M., 2026. ZnO Nanowires for Ultraviolet Detection: Recent Developments, Challenges, and Future Outlook. *Advanced Electronic Materials*, p.e70503.

[2] Chen, A., Li, Y., Zhang, J., Tong, H., Xie, Z., Miao, S., Zhou, Y. and Shen, H., 2026. Self-Powered ZnO Quantum Dot/Si Photodetector with Light-Trapping Inverted Pyramid Structure and High Detectivity. *ACS Applied Nano Materials, 9(17)*, pp.7634-7642.

[3] Ahsan, U., Elahi, E., Sattar, A., Sarkar, K.J., Asad, M., Mustafa, H., Irfan, M., Sabar, M.A. and Sofer, Z., 2026. Advances in visible and ultraviolet self-powered photodetectors: exploring 2D materials and Janus heterostructures. *Nanoscale, 18(2)*, pp.537-574.

[4] Ülkü, A., Potztal, R., Blaettler, T., Küpçü, C.T., Besserer, R., Bertsch, D., Strüning, T. and Huber, S., 2026. Ultraviolet photoresponse properties of ZnO: N/p-Si and ZnO/p-Si heterojunctions. *Reduction in Dark Current in Photodiodes: A Review. Micromachines, 17(4)*, p.458.

[5] Soylu, M. and Simsek, E., 2026. The electro-optic and photonic properties of TU: ZnO thin-film-based photodiodes prepared by sol-gel spin coating. *Journal of Materials Science: Materials in Electronics, 37(4)*, p.309.

[6] Abdelhamid Shahat, M., Khamees, A.S., Ghitas, A. and Ezzat, H.A., 2026. Highly sensitive hierarchically structured Si-based UV sensor-photodetectors via optimized ZnO-Al_2O_3 nanocomposite architectures. *Scientific Reports, 16(1)*, p.8497.

[7] Shang, T., Li, C., Shi, Y., Sang, D., Zhang, Z., Li, H. and Wang, Q., 2026. Current progress of excellent photodetectors based on novel semiconductor nanomaterials. *Nanomaterials, 16(9)*, p.549.

[8] Peng, Y., Xu, X., Zheng, Z., Lu, Y., Chen, N., Wang, Y., Xu, S., Lv, W., Sun, L. and Wang, Y., High performance photodiodes based on p-Si/ZnO/copper phthalocyanine double heterojunctions. ZnO/copper phthalocyanine double heterojunctions.

[9] Pasdar, M., Azimirad, R. and Nayeri, F.D., 2025. Improving the performance of UV photodiode detectors by changing the dimensions of ZnO nanorods. *Optics Communications, 584*, p.131681.

[10] Mun, D.H. and Ha, J.S., 2013. The effect of precursor concentration on ZnO nanorod grown by low-temperature aqueous solution method. *Journal of the Microelectronics and Packaging Society, 20(1)*, pp.33-37.

[11] Tong, F., Kim, K., Wang, Y., Thapa, R., Sharma, Y., Modic, A., Claude Ahyi, A., Issacs-Smith, T., Williams, J., Ahn, H. and Park, H., 2012. Growth of ZnO nanorod arrays on flexible substrates: effect of precursor solution concentration. *International Scholarly Research Notices, 2012(1)*, p.651468.

[12] Satpathy, S.K., Panigrahi, U.K., Panda, S.K., Thiruvengadam, V., Biswal, R., Luyten, W. and Mallick, P., 2021. Influence of Gd doping on morphological, toxicity and magnetic properties of ZnO nanorods. *Materials today communications, 28*, p.102725.

[13] Seydioglu, T., Kurnaz, S., Tokeer, E.A., Yildirim, G. and Ozturk, O., 2024. Effect of foreign impurity and growth temperatures on hexagonal structure and fundamental properties of ZnO nanorods. *Microscopy Research and Technique, 87(11)*, pp.2687-2700.

[14] Wu, W.H., Chao, C.H., Hung, S.C. and Lin, C.F., 2010, August. Compact ZnO nanorods composed film by re-growth of ZnO nanorods and Ar plasma treatment. *In 10th IEEE International Conference on Nanotechnology*, (pp. 525-528). IEEE.

[15] Ni, Y.H., Wei, X.W., Hong, J.M., and Ye, Y., 2005. Hydrothermal preparation and optical properties of ZnO nanorods. *Materials Science and Engineering: B, 121(1-2)*, pp. 42-47.

[16] Huang, N., Shu, J., Wang, Z., Chen, M., Ren, C., and Zhang, W., 2015. One-step pyrolytic synthesis of ZnO nanorods with enhanced photocatalytic activity and high photostability under visible light and UV light irradiation. *Journal of Alloys and Compounds, 648*, pp. 919-929.

[17] Yi, X.Y., Ma, C.Y., Yuan, F., Wang, N., Qin, F.W., Hu, B.C. and Zhang, Q.Y., 2017. Structural, morphological, photoluminescence and photocatalytic properties of Gd-doped ZnO films. *Thin Solid Films, 636*, pp.339-345.

[18] Oprea, O., Vasile, O.R., Voicu, G., Craciun, L. and Andronescu, E., 2012. PHOTOLUMINESCENCE, MAGNETIC PROPERTIES AND PHOTOCATALYTIC ACTIVITY OF Gd^{3+} DOPED ZnO NANOPARTICLES. *Digest Journal of Nanomaterials & Biostructures (DJNB)*, 7(4).

[19] Batvandi, F. and Eshghi, H., 2024. Visible light photoresponse properties of Ag/n-ZnO-NRs/p-Si/Al photodiodes, the influence of optimal ZnO precursor concentration via CBD method. *Sensors and Actuators A: Physical, 370*, p.115283.

[20] Vijayaprasath, G., Murugan, R., Hayakawa, Y. and Ravi, G., 2016. Optical and magnetic studies on Gd doped ZnO nanoparticles synthesized by co-precipitation method. *Journal of Luminescence, 178*, pp.375-383.

[21] Yi, X.Y., Ma, C.Y., Yuan, F., Wang, N., Qin, F.W., Hu, B.C. and Zhang, Q.Y., 2017. Structural, morphological, photoluminescence and photocatalytic properties of Gd-doped ZnO films. *Thin Solid Films, 636*, pp.339-345.

[22] Abuelsamen, A.A., Mahmud, S., Seeni, A., Kaus, N.H.M. and Farhat, O.F., 2017. Effects of precursor concentrations on the optical and morphological properties of ZnO nanorods on glass substrate for UV photodetector. *Superlattices and Microstructures, 111*, pp.536-545.

[23] Mazhdi, M. and Tafreshi, M.J., 2018. The effects of gadolinium doping on the structural, morphological, optical, and photoluminescence properties of zinc oxide nanoparticles prepared by co-precipitation method. *Applied Physics A, 124(12)*, p.863.

[24] Bindu, P. and Thomas, S., 2014. Estimation of lattice strain in ZnO nanoparticles: X-ray peak profile analysis. *Journal of Theoretical and Applied Physics, 8*, pp. 123-134.

[25] Baturay, S., Ocak, Y.S. and Kaya, D., 2015. The effect of Gd doping on the electrical and photoelectrical properties of Gd: ZnO/p-Si heterojunctions. *Journal of Alloys and Compounds, 645*, pp.29-33.

[26] Liu, J., Xie, S., Chen, Y., Wang, X., Cheng, H., Liu, F. and Yang, J., 2011. Homoepitaxial regrowth habits of ZnO nanowire arrays. *Nanoscale research letters, 6(1)*, p.619.

[27] Nam, G., Kim, S., Jo, E., Kim, G., Leem, J.Y., Son, J.S. and Kim, S.O., 2017. A regrowth method for the fabrication of high-quality ZnO films and their application in fast-response UV sensors. *Journal of the Korean Physical Society, 71(1)*, pp.47-53.

[28] Sett, S. and Raychaudhuri, A.K., 2020. Effective separation of photogenerated electronhole pairs by radial field facilitates ultrahigh photoresponse in single semiconductor nanowire photodetectors. *The Journal of Physical Chemistry C, 124(41)*, pp.22808-22816.

[29] Kim, H.Y., Kim, J.H., Park, M.O. and Im, S., 2001. Photoelectric, stoichiometric and structural properties of n-ZnO film on p-Si. *Thin Solid Films, 398*, pp.93-98.

[30] Ozel, K., 2024. Strain-induced photoresponsivity in gallium-doped ZnO thin film based UV photodetectors. *Sensors and Actuators A: Physical, 366*, p.114953.

[31] Lee, J.Y., Choi, Y.S., Kim, J.H., Park, M.O. and Im, S., 2002. Optimizing n-ZnO/p-Si heterojunctions for photodiode applications. *Thin solid films, 403*, pp.553-557.

[32] Badran, R.I., Umar, A., Al-Heniti, S., Al-Hajry, A. and Al-Harbi, T., 2010. Synthesis and characterization of zinc oxide nanorods on silicon for the fabrication of p-Si/n-ZnO heterojunction diode. *Journal of Alloys and Compounds, 508(2)*, pp.375-379.

[33] Alwadai, N., Haque, M.A., Mitra, S., Flemban, T., Pak, Y., Wu, T. and Roqan, I., 2017. High-performance ultraviolet-to-infrared broadband perovskite photodetectors achieved via inter-/intraband transitions. *ACS applied materials & interfaces, 9(43)*, pp.37832-37838.

[34] Virt, I. and Padalka, I., 2026. Modeling of a photodiode structure based on a heterojunction ZnO/Si. *Technology and design in electronic equipment, (1)*, pp.17-31.

[35] Nagpal, K., Rauwel, E., Ducroquet, F., Glard, I. and Rauwel, P., 2024. Fabrication and evaluation of figures of merit of ZnO polymer-based hybrid UV photodiodes. *APL Materials*, 12(6).

[36] Muhammad, W., Nam, K., Seo, S. and Kim, S.D., 2022. Role of seed layer crystalline quality in photoresponse performance of hydrothermally grown ZnO nanorods. *International Journal of Molecular Sciences, 23(17)*, p.9541.

[37] Sahare, P.D., Kumar, S., Kumar, S. and Singh, F., 2018. n-ZnO/p-Si heterojunction nanodiodes based sensor for monitoring UV radiation. *Sensors and Actuators A: Physical, 279*, pp.351-360.

[38] Fu, Q.M., Yao, Z.C., Peng, J.L., Zhao, H.Y., Ma, Z.B., Tao, H., Tu, Y.F., Zhou, D. and Tian, Y., 2020. Enhanced photoresponse in ZnO nanorod array/p-GaN self-powered ultraviolet photodetectors via coupling with CuO nanostructures. *Materials Research Express, 7(1)*, p.015063.

[39] Pathinti, R.S., Thyda, L., Thangaraju, K. and Vallamkondu, J., 2025. Novel self-powered UV photodetectors based on nematic liquid crystal integrated with ZnO nanorods. *Journal of Molecular Liquids, 425*, p.127127.

[40] Al-Hardan, N.H., Jalar, A., Hamid, M.A., Keng, L.K., Ahmed, N.M. and Shamsudin, R., 2014. A wide-band UV photodiode based on n-ZnO/p-Si heterojunctions. *Sensors and Actuators A: Physical, 207*, pp.61-66.

[41] Jeong, I.S., Kim, J.H. and Im, S., 2003. Ultraviolet-enhanced photodiode employing n-ZnO/p-Si structure. *Applied physics letters, 83(14)*, pp.2946-2948.

[42] Fu, S., Xi, W., Ren, J., Wei, H. and Sun, W., 2024. Study on the photocatalytic properties of metalorganic framework-derived C-, N-Co-doped ZnO. *Materials, 17(4)*, p.855.

[43] Tarwal, N.L., Patil, K.V., Redekar, R.S., Bhoite, A.A., Janakar, P.M. and Shirage, P.M., 2024. Structural, functional, morphological, and photoluminescence properties of spin coated nanostructured ZnO thin films. *Journal of Materials Science: Materials in Electronics, 35(36)*, p.2283.

[44] Mahdizadeh, R., Sangpour, P. and Emrooz, H.B.M., 2025. Surface texture dependency of photocatalytic behavior of facile synthesized mesoporous ZnS-ZnO heterostructure under LED illumination. *Scientific Reports, 15(1)*, p.30272.

Funding

The authors received no specific funding for this work.

Author contributions statement

R.A. and F.D.N. provided materials and equipment. F.A.B. reviewed the manuscript and provided comments. S.B. performed the initial SEM imaging of the samples. S.S.M. conducted the circuit-level and electronic testing on selected samples.